H1prelim-19-013
April 2019

A determination of diffractive parton distribution functions from H1 inclusive diffractive deep-inelastic scattering data and H1 diffractive dijet cross section data in next-to-next-to-leading order QCD

H1 Collaboration

Abstract

A new combined fit of diffractive parton distribution functions (DPDFs) to the H1 inclusive neutral-current and dijet production data in diffractive deep-inelastic scattering (DDIS) at next-to-next-to-leading order accuracy (NNLO) is presented. Compared to the previous HERA fits, the presented study includes the high-precision H1 HERA-II data, which represents 40 times higher luminosity for inclusive DDIS data sample and 6 times higher luminosity for the jet data, than previous studies by H1. In addition to the inclusive DDIS data at the nominal centre-of-mass energy $\sqrt{s} = 319$, also the inclusive data at 252 and 225 GeV are included into the fit. The inclusion of the most comprehensive dijet cross section data , together with their NNLO predictions, provide enhanced constraints to the gluon component of the DPDF. The extracted DPDFs are compared to the alternative existing DPDFs at NLO accuracy, and are used to predict cross sections for a large number of the available dijet measurements.

Submitted to DIS19 conference, Torino

1 Data selection

For the present analysis measurements of jet cross sections and inclusive DDIS cross sections in lepton-proton collisions performed by the H1 experiment at HERA are exploited. Compared to the previous H1 fits [1,2] which where based on the HERA I data from years 1996-1997, the new fit includes HERA-II data for both inclusive DDIS and jet production in DDIS. These data has about 40 times higher luminosity in case of inclusive production and 6 times higher for the dijets. These data covers the region of $|t| < 1\,\mathrm{GeV}^2$ of the proton four-momentum transfer and $M_Y < 1.6\,\mathrm{GeV}$. For the present study, data based on the large rapidity gap selection method are used, and the selected inclusive neutral-current DDIS data samples are summarised in table 1.

Data set [ref.]	$\sqrt{s}$ [GeV]	int. $\mathcal{L}$ [pb^{-1}]	DIS kinematic range
H1comb-LRG	319	336.6	$8.5 < Q^2 < 1600\,\mathrm{GeV}^2$
H1-LowE-252	252	5.2	$8.5 < Q^2 < 44\,\mathrm{GeV}^2$
H1-LowE-225	225	8.5	$8.5 < Q^2 < 44\,\mathrm{GeV}^2$

Table 1: Summary of inclusive NC DDIS data samples selected for the present DPDF fit. On the of the $Q^2 > 8.5\,\mathrm{GeV}^2$ cut the $M_X > 2\,\mathrm{GeV}$ is applied to avoid resonance region.

The combined data set H1comb-LRG [3] was obtained from a combination of six individual data sets as summarised in table 2. Cross section measurements at reduced centre-of-mass energies of 225 and 252 GeV [4] are used here for the first time in a diffractive PDF fit.

Data set [ref.]	$\sqrt{s}$ [GeV]	int. $\mathcal{L}$ [pb^{-1}]	DIS kinematic range
1999 MB	319	3.5	$3 < Q^2 < 25\,\mathrm{GeV}^2$
1999-2000	319	34.3	$10 < Q^2 < 105\,\mathrm{GeV}^2$
2004-2007	319	336.6	$10 < Q^2 < 105\,\mathrm{GeV}^2$
1997 MB	300	2.0	$3 < Q^2 < 13.5\,\mathrm{GeV}^2$
1997 all	300	10.6	$13.5 < Q^2 < 105\,\mathrm{GeV}^2$
1999-2000	319	61.6	$133\,\mathrm{GeV}^2 < Q^2$

Table 2: Summary of the individual data sets that went into the H1comb-LRG data set, which is then selected for the present DPDF fit.

In addition to the inclusive NC DDIS data, also cross sections for dijet production in NC DDIS [5] are considered for the present DPDF fit. Albeit there is considerable variety of different measurements, for the present fit we select only only the HERA-II dijet cross section data based on LRG selection, due to its outstanding statistical uncertainty in comparison to other analysis, and since this analysis was performed double-differentially as a function of Q^2 and the average transverse momentum of the two leading jets, $\langle P_\mathrm{T} \rangle$. The selected dijet cross section data is summarised in table 3. Further data on diffractive dijet production [2, 5–9] are also compared to predictions based on the new fit.

Data Set	$\mathcal{L}$	**DIS**	**Dijet**	**Diffractive**
	$[\mathrm{pb}^{-1}]$	**range**	**range**	**range**
H1 LRG (HERA 2) [5]	290	$4 < Q^2 < 100\,\mathrm{GeV}^2$	$p_{\mathrm{T}}^{*,\mathrm{jet1}} > 5.5\,\mathrm{GeV}$	$x_{I\!P} < 0.03$
	($\sim$15000ev)	$0.1 < y < 0.7$	$p_{\mathrm{T}}^{*,\mathrm{jet2}} > 4.0\,\mathrm{GeV}$	$\lvert t\rvert < 1\,\mathrm{GeV}^2$
			$-1 < \eta_{\mathrm{lab}}^{\mathrm{jet}} < 2$	$M_{\mathrm{Y}} < 1.6\,\mathrm{GeV}$

Table 3: Summary of the dijet data sets used in the present DPDF analysis. From the H1 LRG (HERA 2) dijet measurement, the double-differential cross sections as functions of Q^2 and $\langle P_{\mathrm{T}}\rangle$ are selected.

2 Tables and figures

Data set	process	χ^2/n_{data}
H1comb-LRG	inclusive NC DDIS	192/191
H1-LowE-225	inclusive NC DDIS	19/12
H1-LowE-252	inclusive NC DDIS	10/13
H1 LRG (HERA 2)	dijet production	12/15
all		235/231
		$[n_{\mathrm{dof}} = 223]$

Table 4: Summary of the partial χ^2 values and the total value of χ^2 for the DPDF fit to inclusive NC DDIS and dijet data in NNLO.

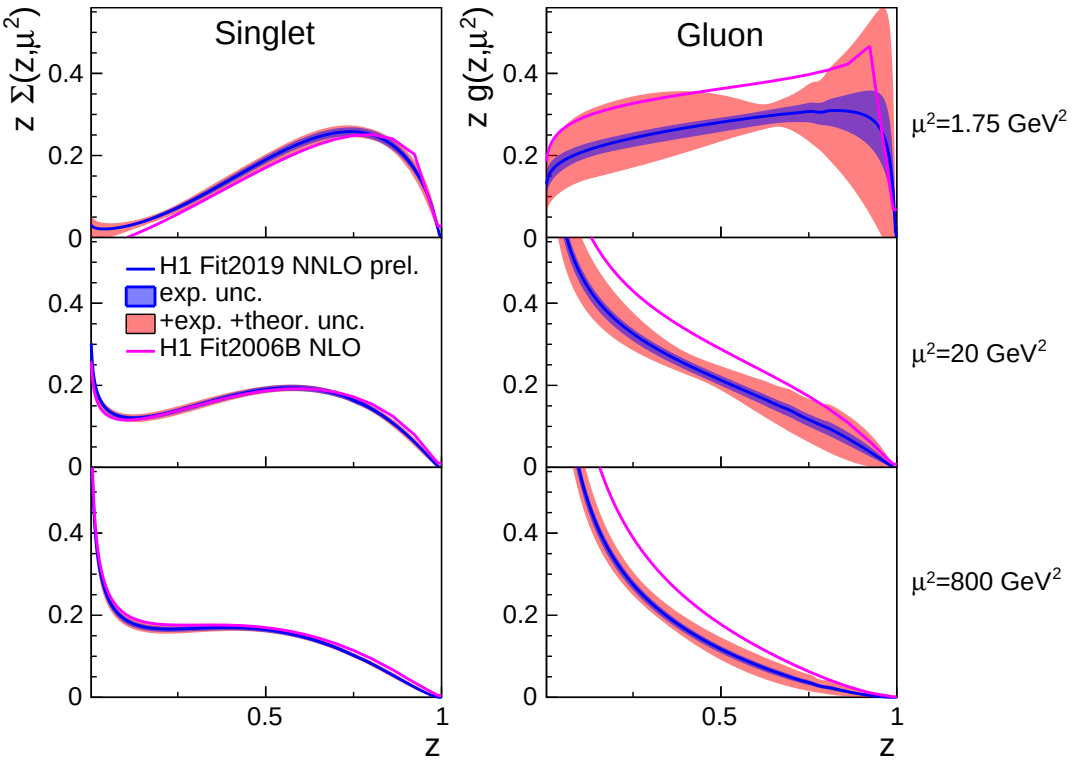

Figure 1: Singlet (left, Σ) and gluon (right, g) distributions of the pomeron in H1 Fit2019 NNLO (prel.) as a function of z for three different values of $\mu_{\rm F}$ at a value of $x_{I\!P} = 0.003$. The inner (dark) error band displays the experimental uncertainty, while the outer (bright) error band displays the full uncertainty, i.e. experimental, parameterisation, model and theoretical uncertainties added in quadrature. The H1 Fit2019 NNLO (prel.) is compared to H1FitB (dashed line), which was obtained in an NLO pQCD fit.

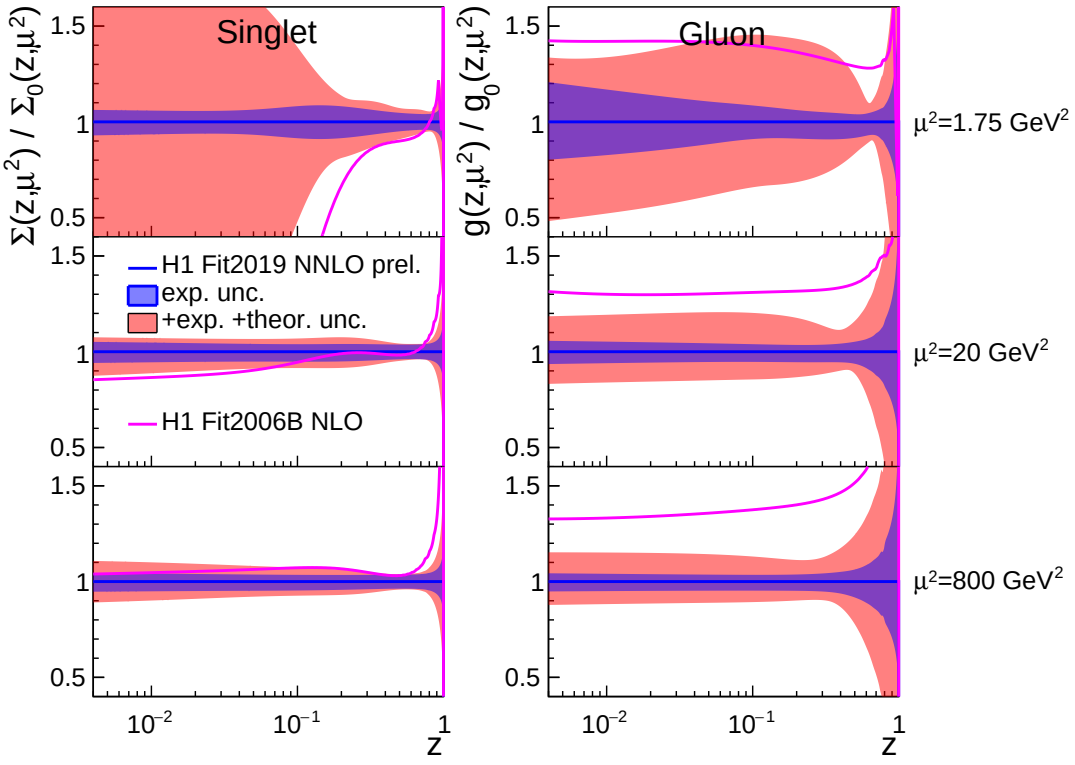

Figure 2: Ratio to H1 Fit2019 NNLO (prel.) as function of $z$for three different values of μ_F at a value of $x_{I\!P} = 0.003$. More details as in fig. 1. Note the logarithmic scale (c.f. fig. 1 with linear scale).

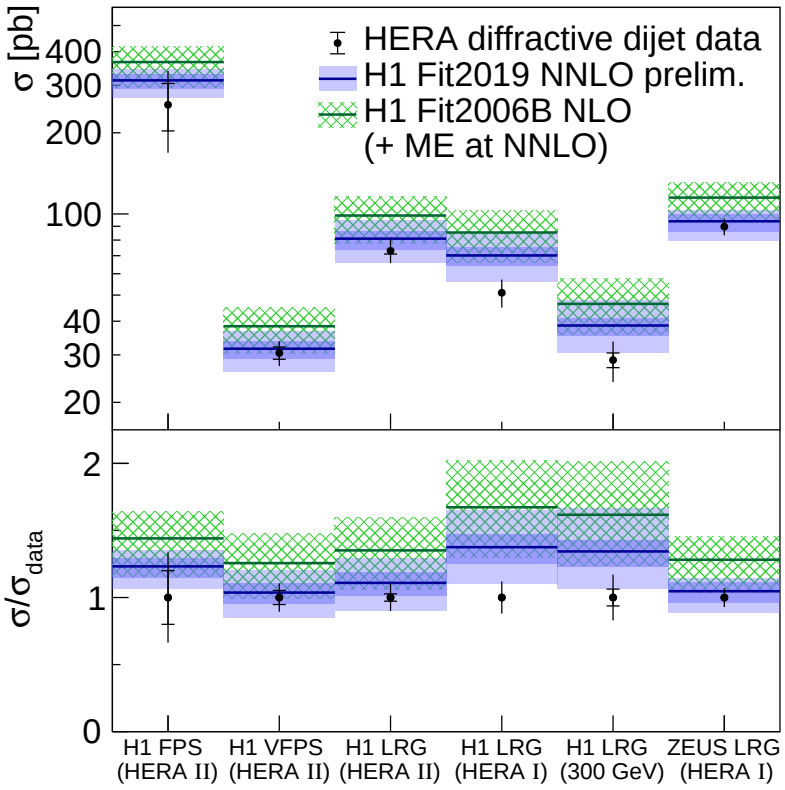

Figure 3: NNLO pQCD predictions (full blue line) using H1 Fit2019 NNLO (prel.) in comparison to the total dijet cross section measured in six different analysis by the H1 or ZEUS collaborations (full circles). The upper panel displays the total cross section, and the lower panel the ratio of the predictions to data. The inner error band (dark blue) displays the DPDF uncertainty of the H1 Fit2019 NNLO (prel.) fit, and the outer error band (light blue) displays the DPDF uncertainty and scale uncertainty added in quadrature. The hatched band displays the DPDF uncertainty and NLO scale uncertainty of the NLO predictions. The inner error of the data displays the statistical uncertainty, and the full error bars displays the total experimental uncertainty. For comparison, NNLO pQCD predictions using the H1FitB NLO PDF are also shown.

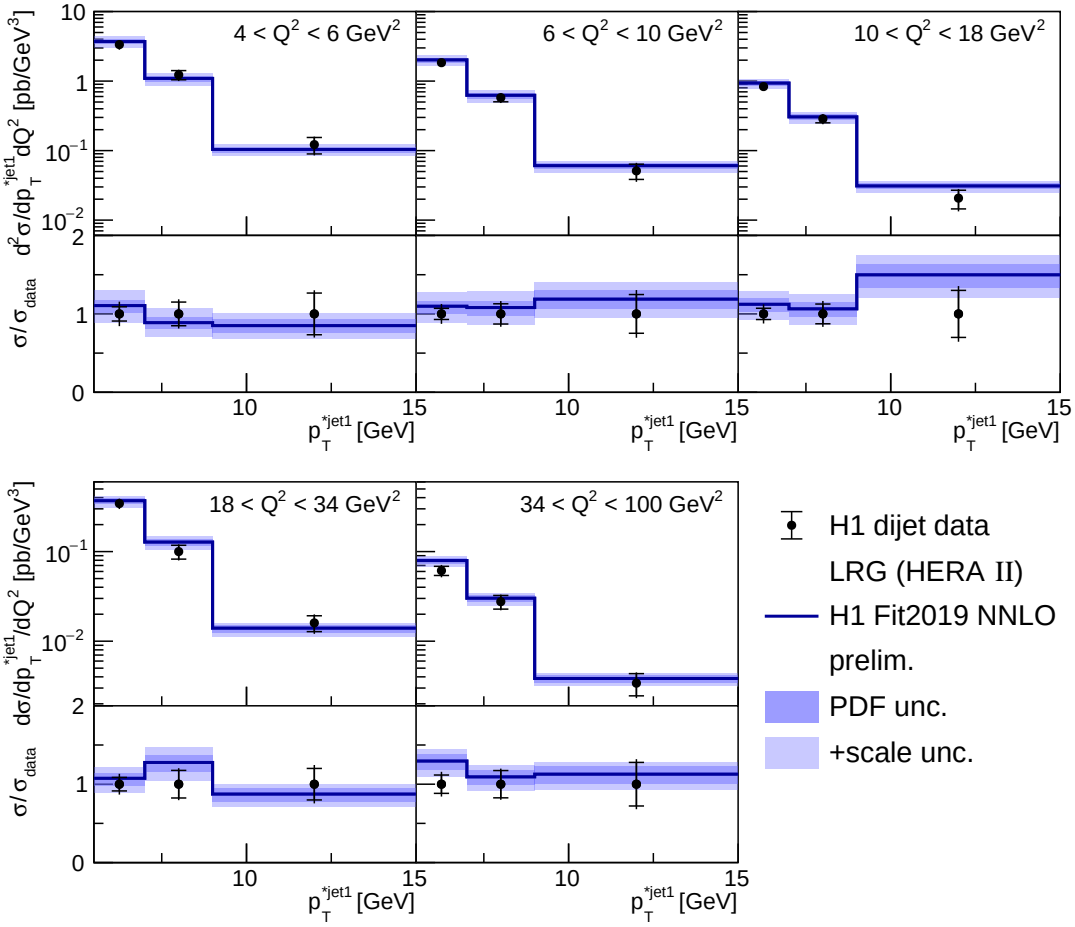

Figure 4: Comparison of NNLO predictions using H1 Fit2019 NNLO (prel.) (full line) to H1 dijet cross section data (full circles) as a function of $\langle P_{\mathrm{T}} \rangle$ for different Q^2 intervals. The inner band indicates the uncertainties associated to the H1 Fit2019 NNLO (prel.). The outer band incorporates the scale uncertainty.

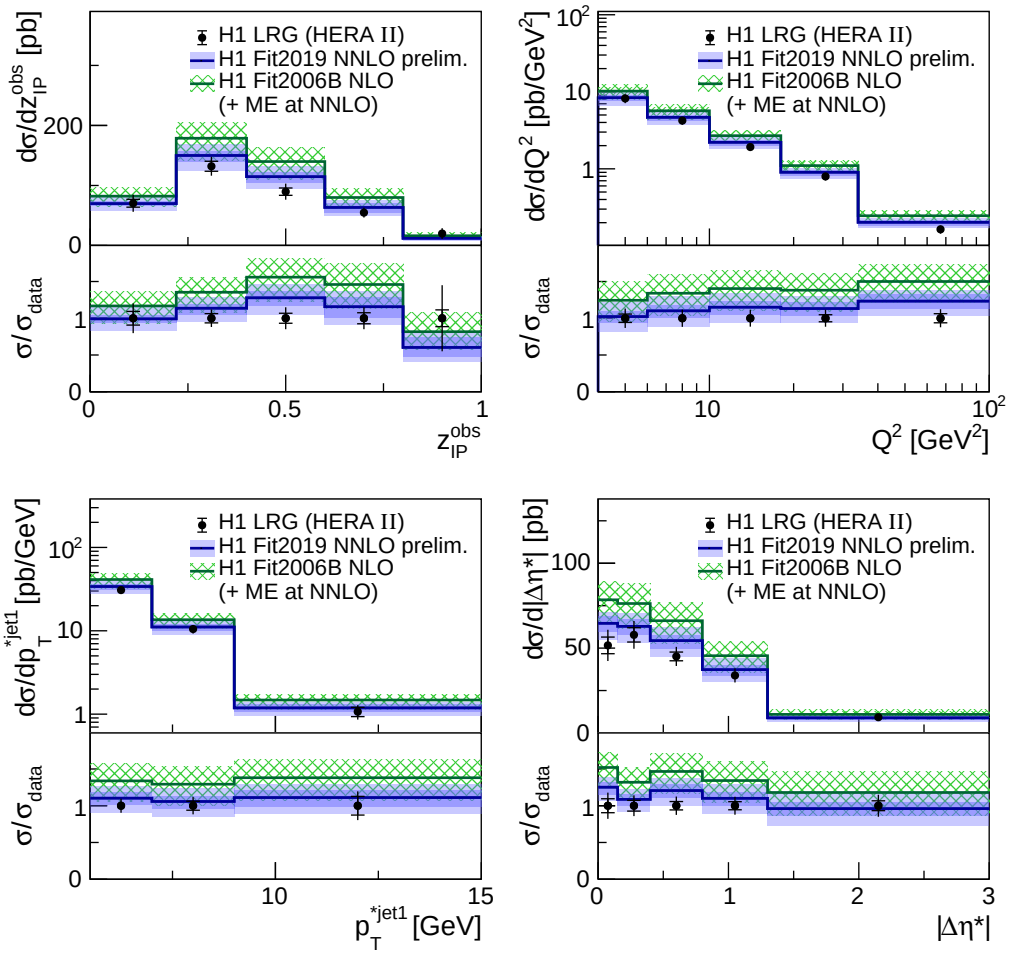

Figure 5: Comparison of NNLO predictions using H1 Fit2019 NNLO (prel.) (full line) to H1 dijet cross section data (full circles) as a function of . The inner band indicates the uncertainties associated to the H1 Fit2019 NNLO (prel.). The outer band incorporates the scale uncertainty.

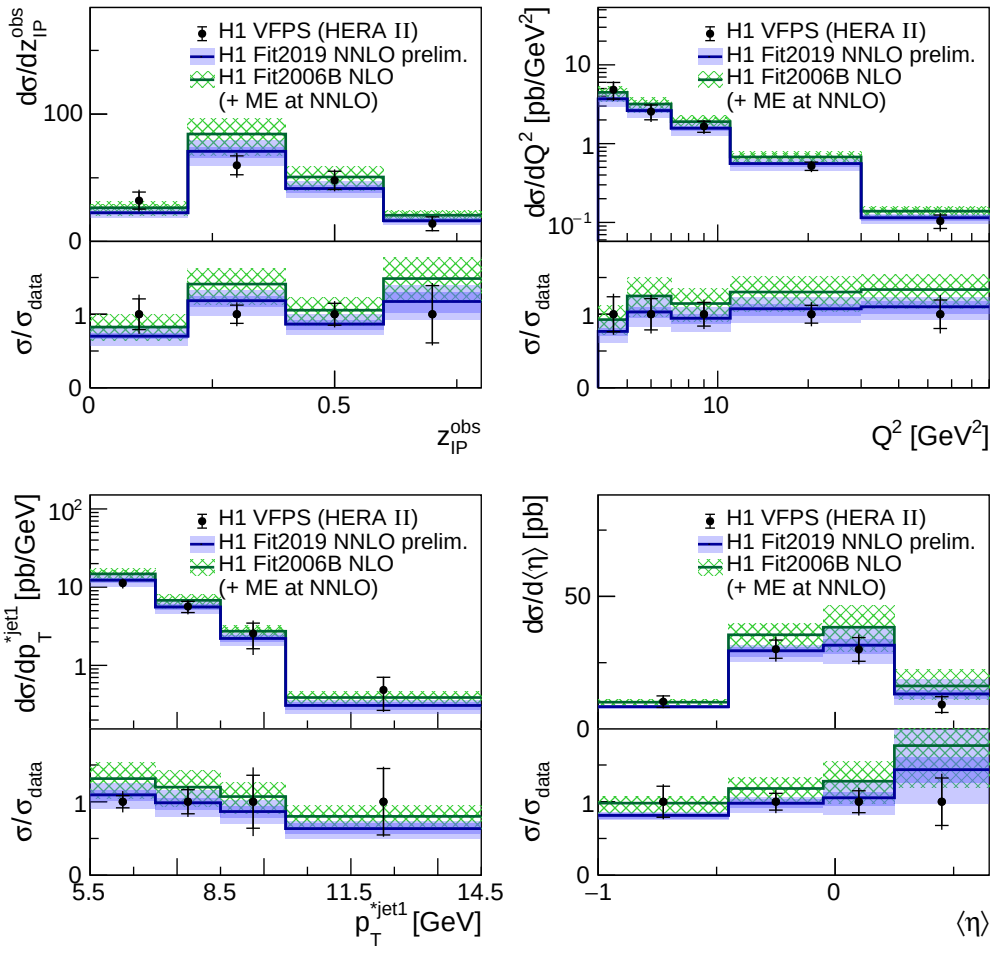

Figure 6: Comparison of NNLO predictions using H1 Fit2019 NNLO (prel.) (full line) to ZEUS dijet cross section data (full circles) as a function of . The inner band indicates the uncertainties associated to the H1 Fit2019 NNLO (prel.). The outer band incorporates the scale uncertainty.

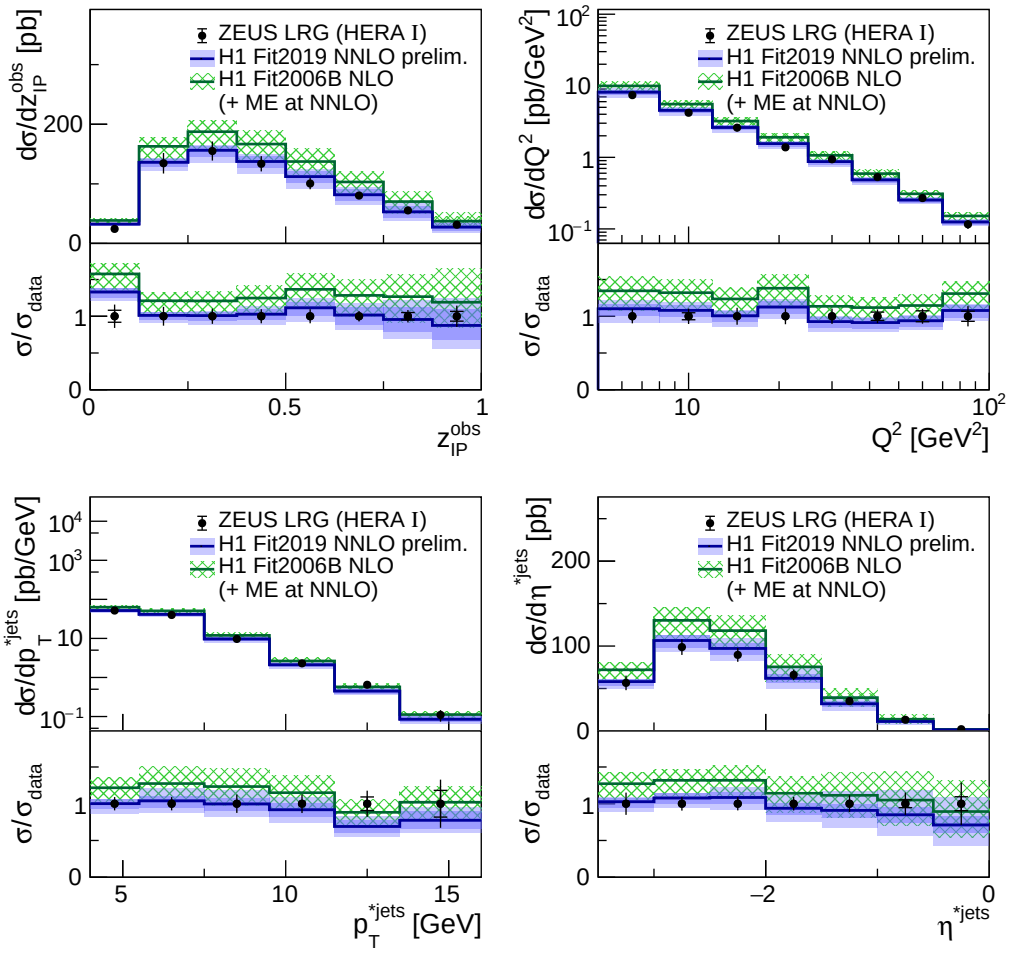

Figure 7: Comparison of NNLO predictions using H1 Fit2019 NNLO (prel.) (full line) to ZEUS dijet cross section data (full circles) as a function of . The inner band indicates the uncertainties associated to the H1 Fit2019 NNLO (prel.). The outer band incorporates the scale uncertainty.

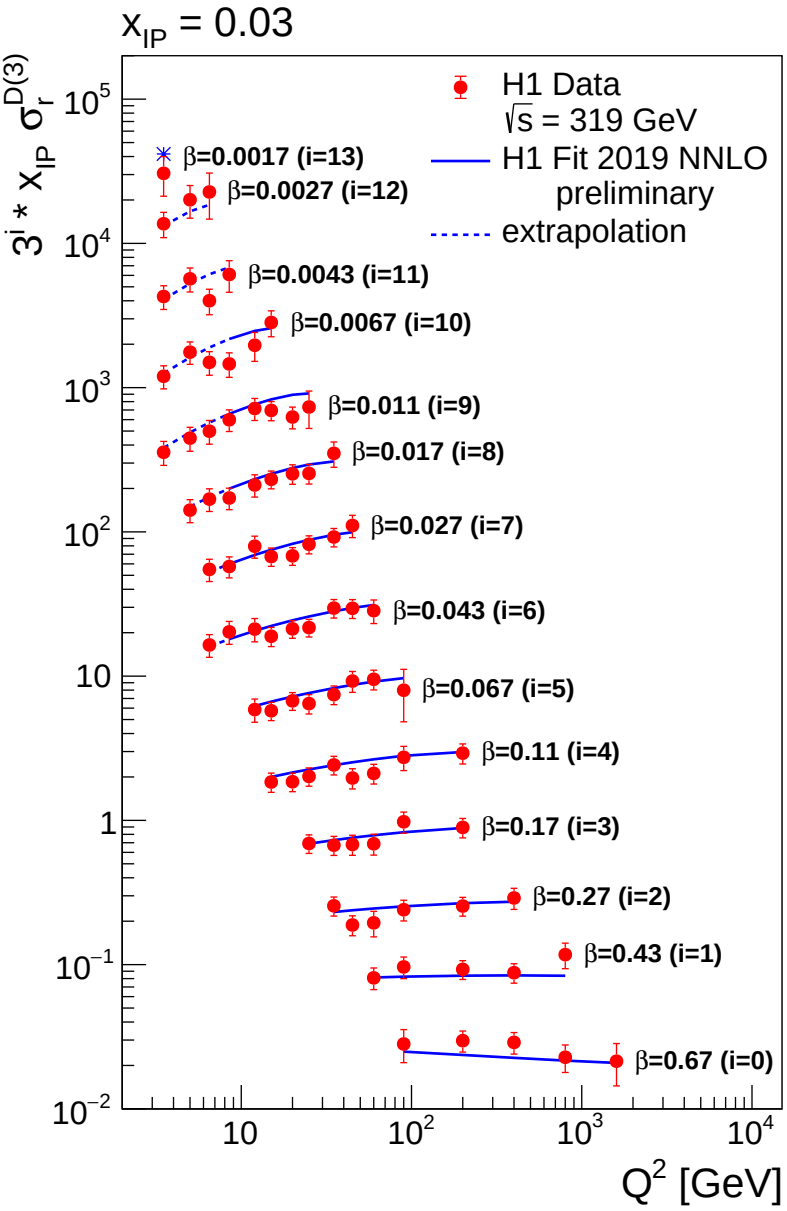

Figure 8: Comparison of (fitted) NNLO predictions using H1 Fit2019 NNLO (prel.) (full line) to H1 combined LRG data at $x_{I\!P} = 0.03$ (full circles) as a function of Q^2. The predictions are extrapolated to data points, which are not included in the H1 Fit2019 NNLO (prel.) fit (dashed line).

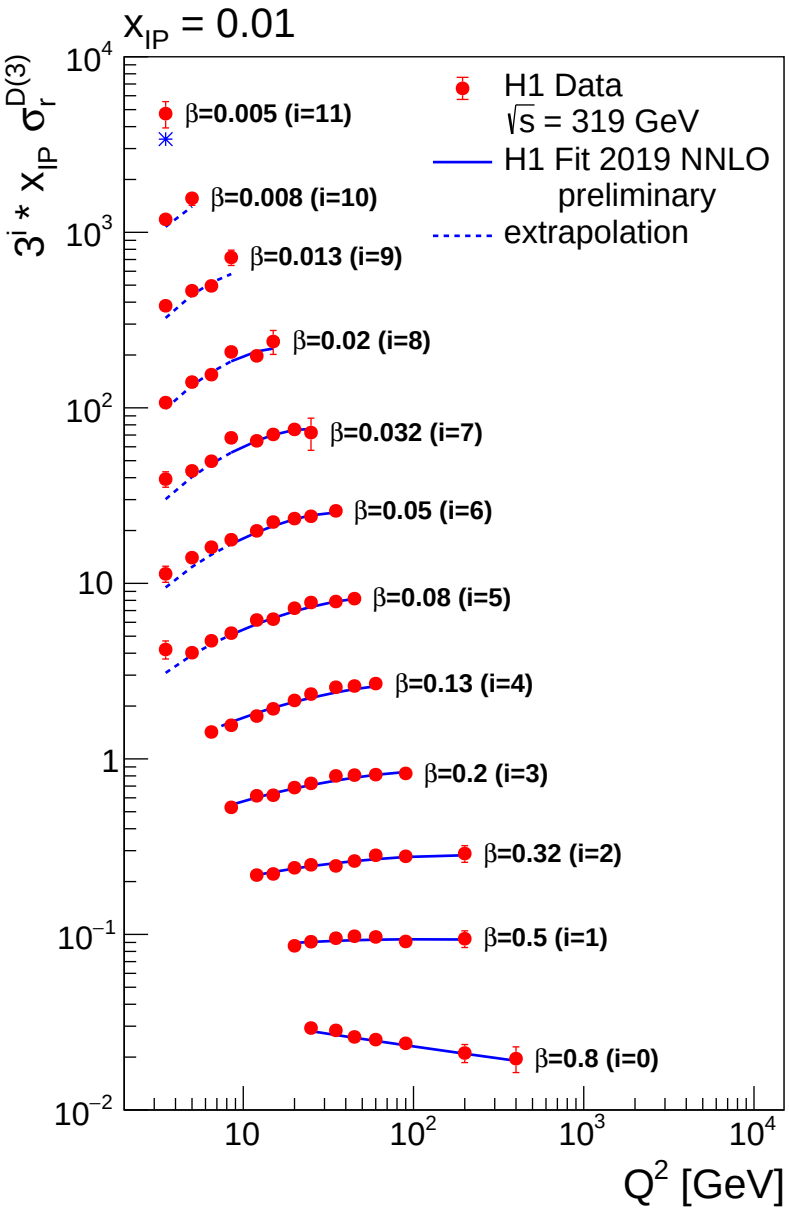

Figure 9: Comparison of (fitted) NNLO predictions using H1 Fit2019 NNLO (prel.) (full line) to H1 combined LRG data as a function of Q^2 at $x_{I\!P} = 0.01$ (full circles). Other details as in fig. 8.

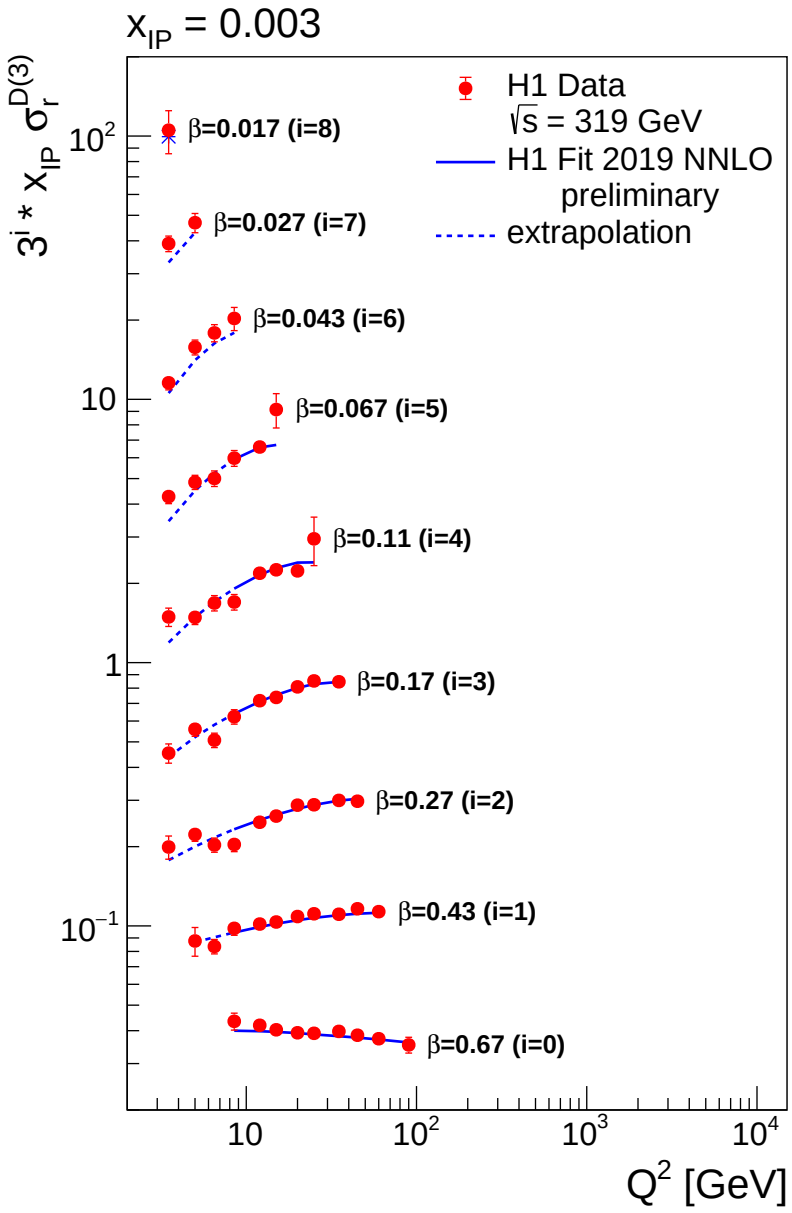

Figure 10: Comparison of (fitted) NNLO predictions using H1 Fit2019 NNLO (prel.) (full line) to H1 combined LRG data as a function of Q^2 at $x_{I\!P} = 0.003$ (full circles). Other details as in fig. 8.

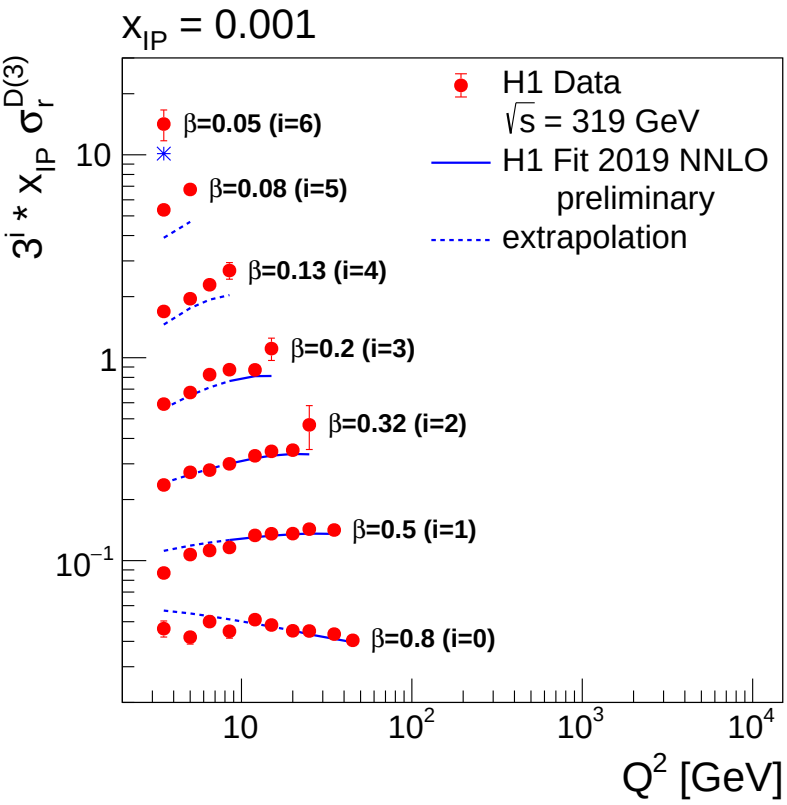

Figure 11: Comparison of (fitted) NNLO predictions using H1 Fit2019 NNLO (prel.) (full line) to H1 combined LRG data as a function of Q^2 at $x_{I\!P} = 0.001$ (full circles). Other details as in fig. 8.

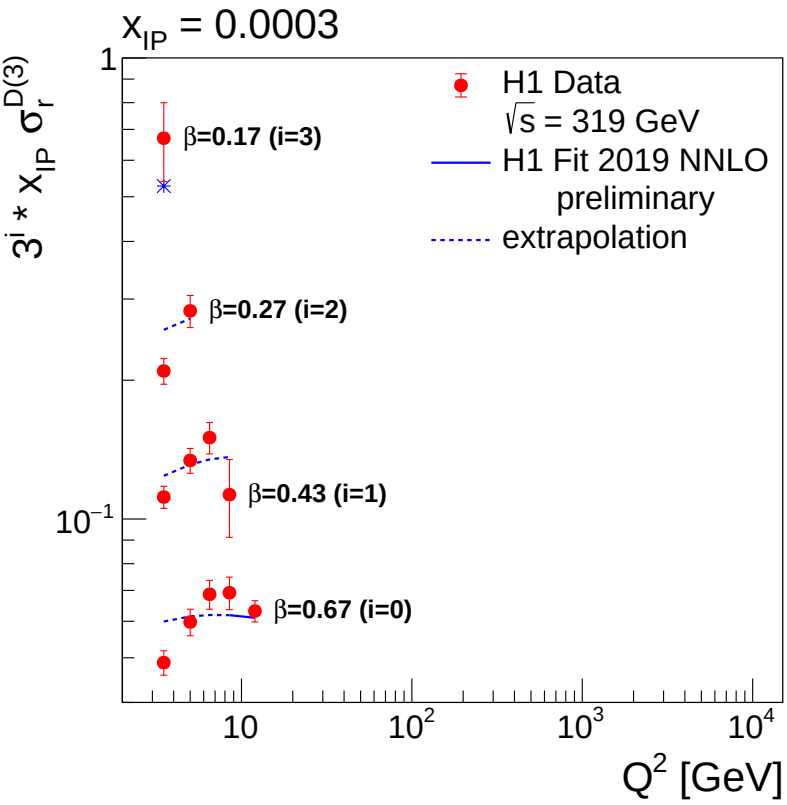

Figure 12: Comparison of (fitted) NNLO predictions using H1 Fit2019 NNLO (prel.) (full line) to H1 combined LRG data as a function of Q^2 at $x_{I\!P} = 0.0003$ (full circles). Other details as in fig. 8.

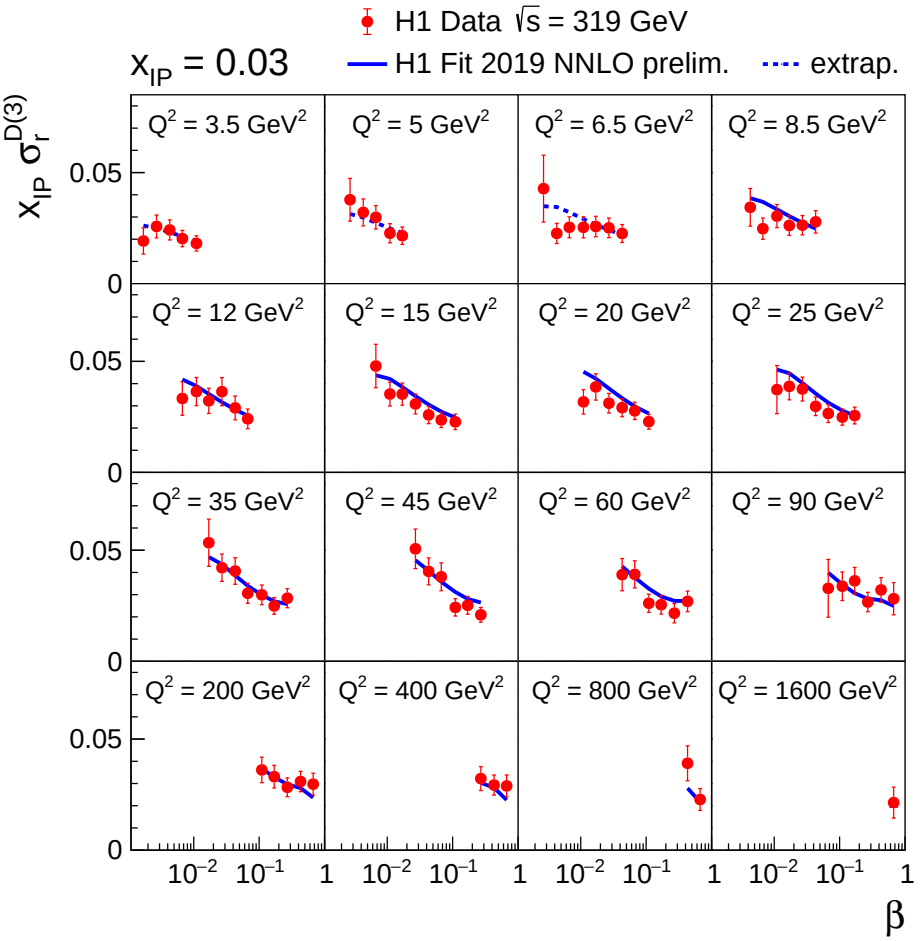

Figure 13: Comparison of (fitted) NNLO predictions using H1 Fit2019 NNLO (prel.) (full line) to H1 combined LRG data as a function of β at $x_{I\!P} = 0.03$ (full circles). Other details as in fig. 8.

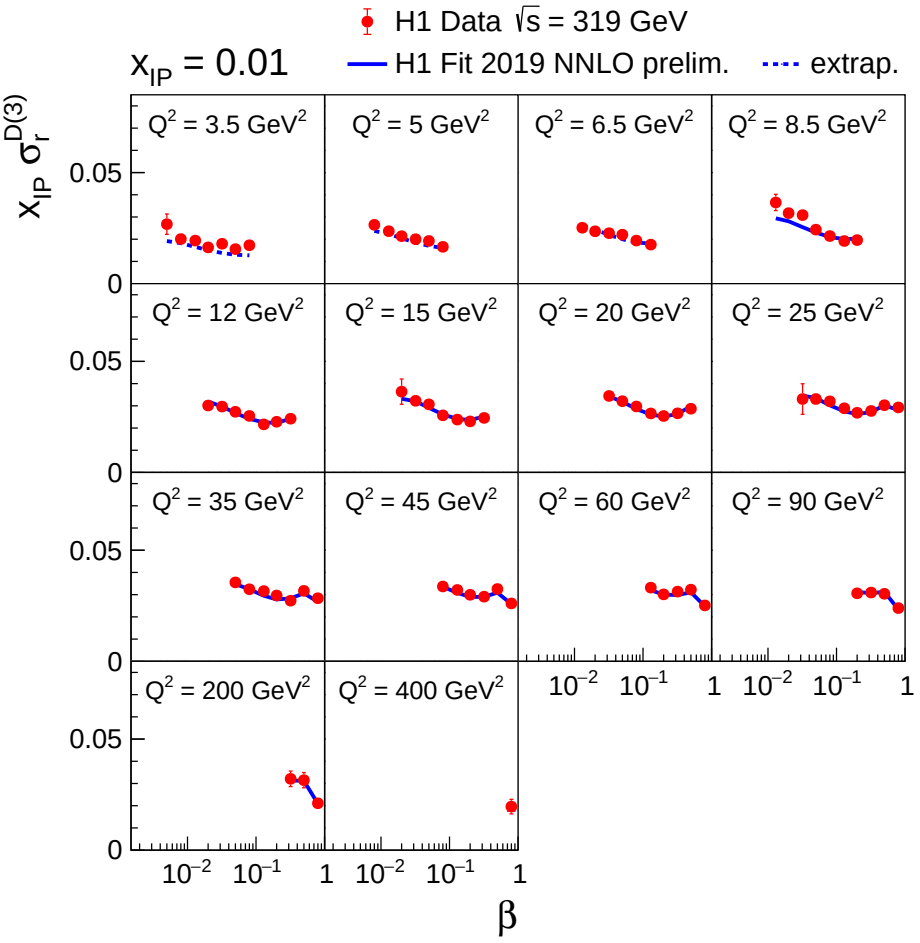

Figure 14: Comparison of (fitted) NNLO predictions using H1 Fit2019 NNLO (prel.) (full line) to H1 combined LRG data as a function of β at $x_{I\!P} = 0.01$ (full circles). Other details as in fig. 8.

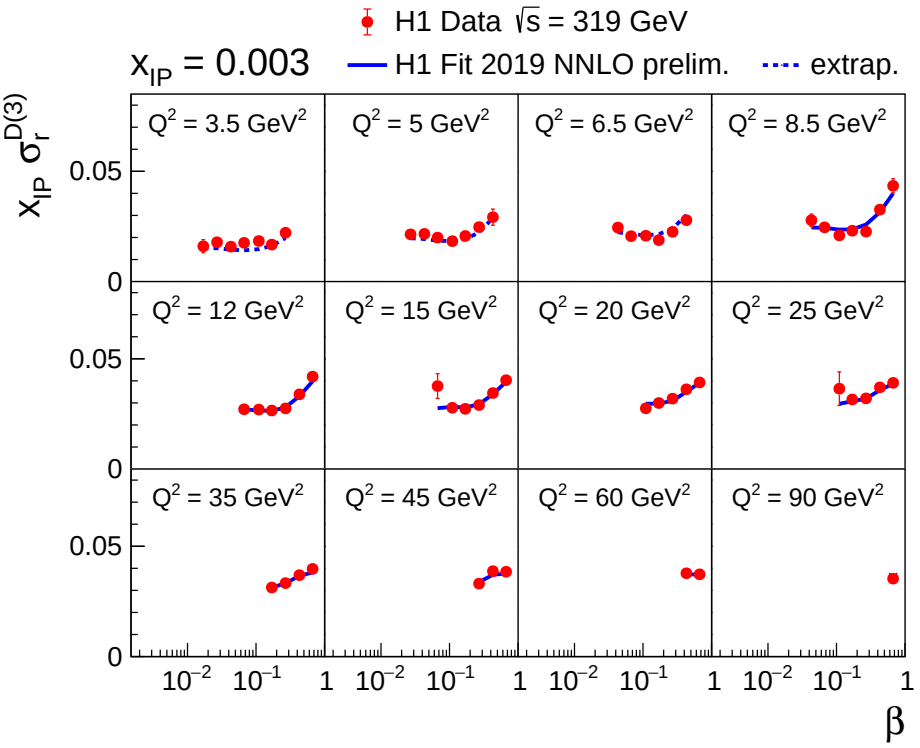

Figure 15: Comparison of (fitted) NNLO predictions using H1 Fit2019 NNLO (prel.) (full line) to H1 combined LRG data as a function of β at $x_{I\!P} = 0.003$ (full circles). Other details as in fig. 8.

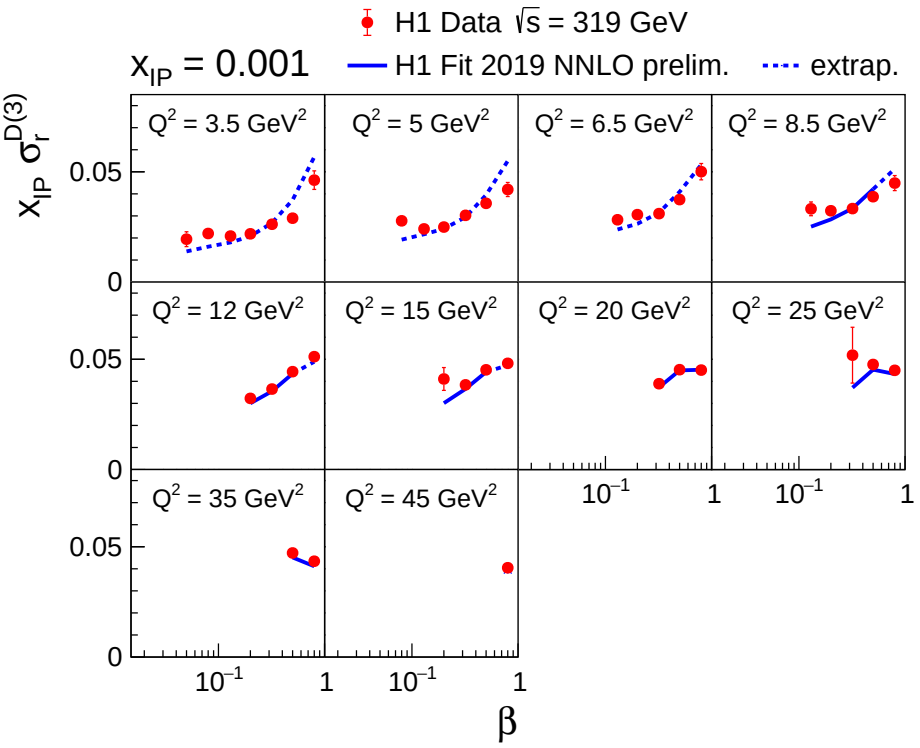

Figure 16: Comparison of (fitted) NNLO predictions using H1 Fit2019 NNLO (prel.) (full line) to H1 combined LRG data as a function of β at $x_{I\!P} = 0.001$ (full circles). Other details as in fig. 8.

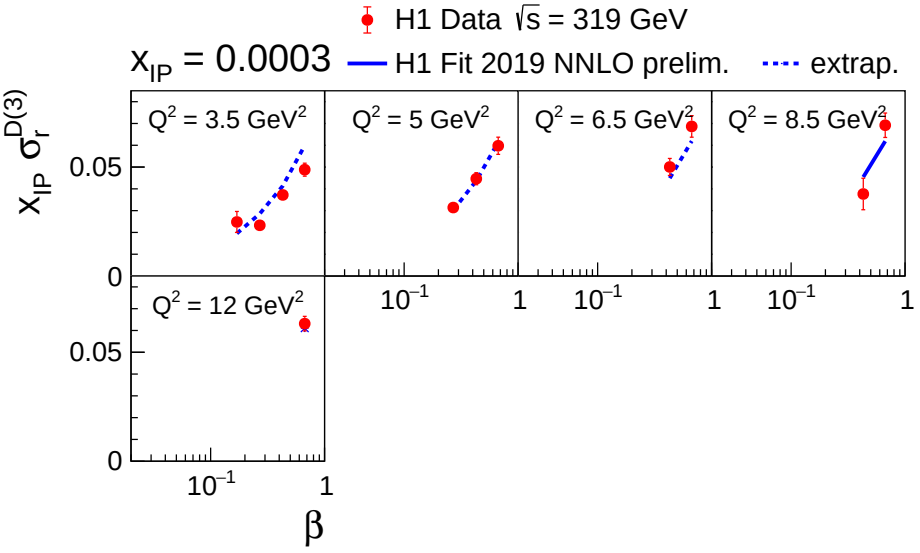

Figure 17: Comparison of (fitted) NNLO predictions using H1 Fit2019 NNLO (prel.) (full line) to H1 combined LRG data as a function of β at $x_{I\!P} = 0.0003$ (full circles). Other details as in fig. 8.

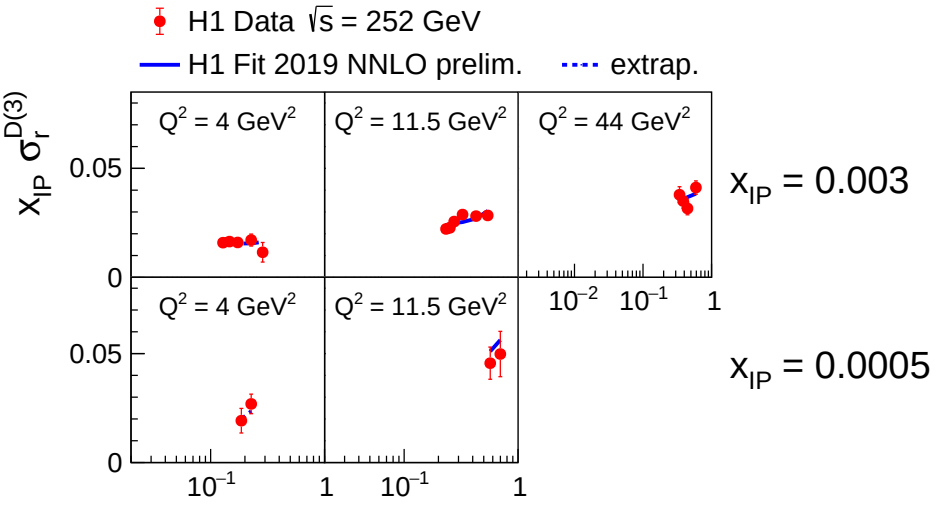

Figure 18: Comparison of (fitted) NNLO predictions using H1 Fit2019 NNLO (prel.) (full line) to H1 LRG data taken with $\sqrt{s} = 252\,\text{GeV}$ at $x_{I\!P} = 0.003$ and $x_{I\!P} = 0.0005$ (full circles) as a function of β. Other details as in fig. 8.

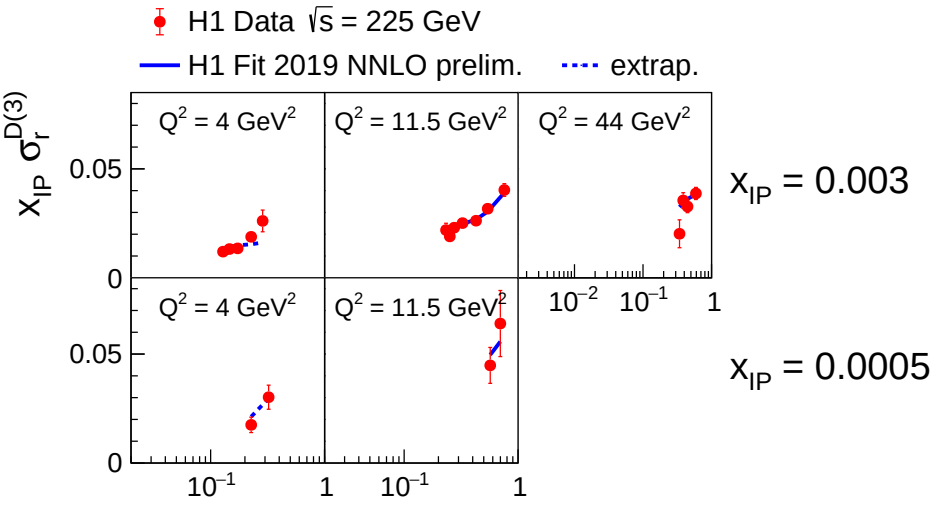

Figure 19: Comparison of (fitted) NNLO predictions using H1 Fit2019 NNLO (prel.) (full line) to H1 LRG data taken with $\sqrt{s} = 225\,\text{GeV}$ at $x_{I\!P} = 0.003$ and $x_{I\!P} = 0.0005$ (full circles) as a function of β. Other details as in fig. 8.

References

[1] H1 Collaboration, A. Aktas *et al.*, *Eur. Phys. J.* C48 (2006) 715, arXiv:hep-ex/0606004.

[2] H1 Collaboration, A. Aktas *et al.*, *JHEP* 10 (2007) 042, arXiv:0708.3217.

[3] H1 Collaboration, F. D. Aaron *et al.*, *Eur. Phys. J.* C72 (2012) 2074, arXiv:1203.4495.

[4] H1 Collaboration, F. D. Aaron *et al.*, *Eur. Phys. J.* C71 (2011) 1836, arXiv:1107.3420.

[5] H1 Collaboration, V. Andreev *et al.*, *JHEP* 03 (2015) 092, arXiv:1412.0928.

[6] H1 Collaboration, C. Adloff *et al.*, *Eur. Phys. J.* C20 (2001) 29–49, arXiv:hep-ex/0012051.

[7] ZEUS Collaboration, S. Chekanov *et al.*, *Eur. Phys. J.* C52 (2007) 813, arXiv:0708.1415. [,671(2007)].

[8] H1 Collaboration, F. D. Aaron *et al.*, *Eur. Phys. J.* C72 (2012) 1970, arXiv:1111.0584.

[9] H1 Collaboration, V. Andreev *et al.*, *JHEP* 05 (2015) 056, arXiv:1502.01683.